

**Perfluoroterephthalate Bridged Complexes with M–M
Quadruple Bonds: (^tBuCO₂)₃M₂(μ-O₂CC₆F₄CO₂)M₂(O₂C^tBu)₃,
where M = Mo or W. Studies of Solid-State, Molecular, and
Electronic Structure and Correlations with Electronic and
Raman Spectral Data**

Bruce E. Bursten,^{*,†} Malcolm H. Chisholm,^{*,†} Robin J. H. Clark,^{*,‡} Steven Firth,[‡]
Christopher M. Hadad,^{*,†} Paul J. Wilson,[†] Patrick M. Woodward,^{*,†} and
Jeffrey M. Zaleski^{*,§}

*Contribution from the Department of Chemistry, The Ohio State University,
100 West 18th Avenue, Columbus, Ohio 43210, Christopher Ingold Laboratories,
University College London, 20 Gordon Street, London WC1H 0AJ, U.K., and
Department of Chemistry, Indiana University, 800 East Kirkwood Avenue,
Bloomington, Indiana 47405*

Received February 19, 2002

Abstract: The compounds [(^tBuCO₂)₃M₂(μ-O₂CC₆F₄CO₂)M₂(O₂C^tBu)₃], M₄PFT, where M = Mo or W, are shown by model fitting of the powder X-ray diffraction data to have an infinite “twisted” structure involving M···O intermolecular interactions in the solid state. The dihedral angle between the M₂ units of each molecule is 54°. Electronic structure calculations employing density functional theory (Gaussian 98 and ADF2000.01, gradient corrected and time dependent) on the model compounds (HCO₂)₃M₂(μ-O₂CC₆F₄CO₂)M₂(O₂CH)₃, where M = Mo or W, reveal that in the gas phase the model compounds adopt planar D_{2h} ground-state structures wherein M₂ δ to bridge π* back-bonding is maximized. The calculations predict relatively small HOMO–LUMO gaps of 1.53 eV for M = Mo and 1.22 eV for M = W for this planar structure and that, when the “conjugation” is removed by rotation of the plane of the C₆F₄ ring to become orthogonal to the M₄ plane, this energy gap is nearly doubled to 2.57 eV for M = Mo and 2.18 eV for M = W. The Raman and resonance Raman spectra of solid M₄PFT and of Mo₄PFT in THF solution are dominated by bands assigned to the bridging perfluoroterephthalate (pft) group. The intensities of certain Raman bands of solid W₄PFT are strongly enhanced on changing the excitation line from 476.5 nm (off resonance) to 676.5 nm, which is on resonance with the W₂ δ → CO₂ (pft) π* transition at ca. 650 nm. The resonance enhanced bands are δ_s(CO₂) (pft) at 518 cm⁻¹ and its first overtone at 1035 cm⁻¹, consistent with the structural change to W₄PFT expected on excitation from the ground to this π* excited state. The electronic transitions for solid Mo₄PFT (lowest at 410 nm) were not accessible with the available excitation lines (457.9–676.5 nm), and no resonance Raman spectra of this compound could be obtained. For Mo₄PFT in THF solution, it is the band at 399 cm⁻¹ assigned to ν(MoMo) which is the most enhanced on approach to resonance with the electronic band at 470 nm; combination bands involving the C₆F₄ ring-stretching mode, 8a, are also enhanced.

Introduction

The linking together of dinuclear units with metal–metal bonds through dicarboxylate ligands, O₂C–X–CO₂, has been most successfully exploited by Cotton et al. who have prepared and structurally characterized numerous examples of dimers, cyclotrimers, and cyclotetramers.¹ The electronic coupling between the M₂ centers is mediated by the nature of the

dicarboxylate bridge. The two CO₂ moieties may be viewed as both the alligator clips and the switch, as shown in our earlier paper on the oxalate bridged compounds (^tBuCO₂)₃M₂(μ-O₂CCO₂)M₂(O₂C^tBu)₃, M₄OXA, where M = Mo or W.² We describe here our studies on the related perfluoroterephthalate bridged complexes (^tBuCO₂)₃M₂(μ-O₂CC₆F₄CO₂)M₂(O₂C^tBu)₃, M₄PFT, where M = Mo or W, which form microcrystalline precipitates from hydrocarbon solutions.³ We address the issues of molecular and electronic structure, and the relationship between these and the Raman, resonance Raman, and electronic spectra of these compounds in the solid state and in solution.

* To whom correspondence should be addressed: bursten@chemistry.ohio-state.edu; chisholm@chemistry.ohio-state.edu; r.j.h.clark@ucl.ac.uk; hadad@chemistry.ohio-state.edu; woodward@chemistry.ohio-state.edu; zaleski@indiana.edu.

[†] The Ohio State University.

[‡] University College London.

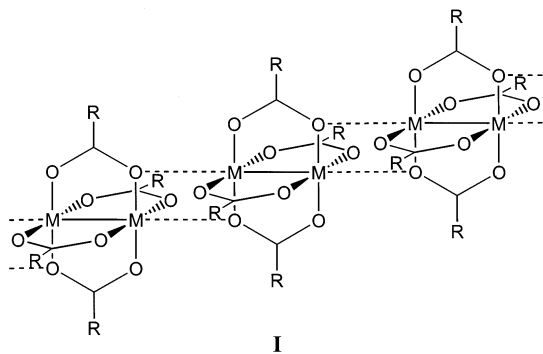
[§] Indiana University.

(1) Cotton, F. A.; Lin, C.; Murillo, C. A. *Acc. Chem. Res.* **2001**, *34*, 759–771.

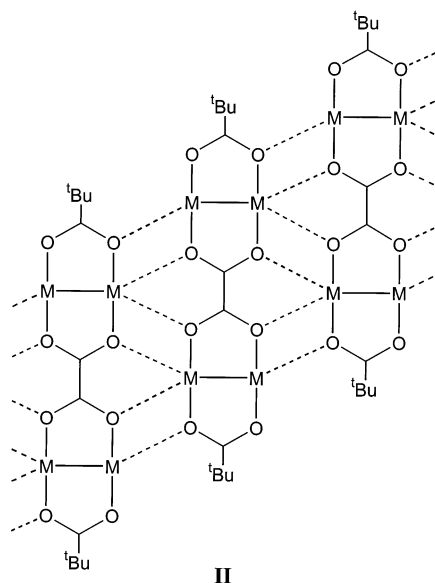
(2) Bursten, B. E.; Chisholm, M. H.; Clark, R. J. H.; Hadad, C. M.; Firth, S.; Macintosh, A. M.; Woodward, P. M.; Wilson, P. J.; Zaleski, J. M. *J. Am. Chem. Soc.* **2002**, *124*, 3050–3063.

(3) Cayton, R. H.; Chisholm, M. H.; Huffman, J. C.; Lobkovsky, E. B. *J. Am. Chem. Soc.* **1991**, *113*, 8709–8724.

The parent compounds $M_2(O_2C^tBu)_4$ form coordination polymers of the type depicted by **I**.^{4,5}



As shown in the earlier paper,² the compounds Mo_4OXA and W_4OXA adopt a variant of this structure wherein both the oxalate and the pivalate (piv) ligands are involved in forming the infinite chain depicted by **II**.



The insertion of a C_6F_4 group into the oxalate C–C bond clearly removes the possibility of forming a polymeric structure akin to **II**, but numerous other three-dimensional structures are possible. We start with the determination of the solid state and molecular structure of the M_4PFT compounds.

Results and Discussion

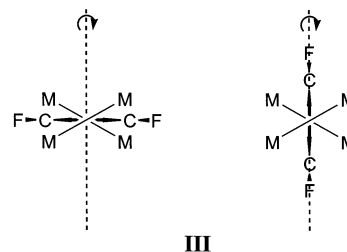
Solid-State Structures. Monochromatic X-ray powder diffraction (XRPD) data were obtained for various samples of both Mo_4PFT and W_4PFT sealed in glass capillaries using a Bruker D8 diffractometer, equipped with an incident beam monochromator. Qualitatively, the data appeared to confirm the two compounds to be isostructural, although unfortunately peaks of the W_4PFT broadened more rapidly than those of Mo_4PFT as a function of 2θ and, consequently, were not suitable for detailed analysis.

The peak positions were determined using the peak fitting routine in the CMPR software package.⁶ The pattern was successfully indexed using both DICVOL⁷ and TREOR,⁸ as

contained within the CRYSFIRE package.⁹ The unit cell was monoclinic with dimensions $a = 21.00 \text{ \AA}$, $b = 5.72 \text{ \AA}$, $c = 20.56 \text{ \AA}$, and $\beta = 101.3^\circ$. The systematic absences were consistent with a C-centered unit cell. For reasons which are fully explained in the Supporting Information, the preferred solution has space group symmetry $C2$.

Peak intensities were extracted using the whole pattern fitting routine in DASH,^{10,11} which is based on the Pawley method.¹² The patterns were also fitted using a whole pattern approach based upon the LeBail method¹³ as implemented in the GSAS software suite.¹⁴ A starting model of the molecular geometry was derived from the optimized gas-phase structure of the model compound $(HCO_2)_3Mo_2(\mu-O_2CC_6F_4CO_2)Mo_2(O_2CH)_3$, determined by density functional theory (DFT) employing the Gaussian 98 package (see later), and replacing the formate protons by *tert*-butyl groups. The structure determination proceeded by means of the simulated annealing optimization algorithm implemented within DASH. In this instance, the location of the molecule was constrained by symmetry, so that the parameters to be optimized included the orientation of the molecule and the torsions at the carboxylates of the PFT group and the *tert*-butyl groups. Finally, a constrained Rietveld refinement was carried out keeping the fractional coordinates of the atoms fixed. The final fit to the experimental diffraction pattern is shown in Figure 1, and the final crystallographic parameters are tabulated and summarized in Table 1. A more detailed account of the structure solution process is given in the Supporting Information.

The crystal structure solution of Mo_4PFT represents a somewhat nonstandard application of DASH^{10,11} in that the location of the molecule is constrained by symmetry. In the space group $C2$, the molecule has a crystallographically imposed 2-fold rotational axis which relates the two halves of the molecule. In an ordered structure, this 2-fold axis must bisect the C_6F_4 ring which can therefore adopt one of two possible orientations, either parallel or perpendicular to the 2-fold axis, both of which are represented in **III**.



Alternatively, the plane of the C_6F_4 group could be disordered over two or more orientations. All three possibilities were

- (6) CMPR was written by Brian Toby and can be obtained free of charge from <http://www.ncnr.nist.gov/programs/crystallography/software/cmpr/>.
- (7) Boultif, A.; Louer, D. J. *Appl. Crystallogr.* **1991**, *24*, 987–993.
- (8) Werner, P. E.; Eriksson, L.; Westdahl, M. J. *Appl. Crystallogr.* **1985**, *18*, 367–370.
- (9) CRYSFIRE was written by Robin Shirley and can be obtained free of charge from <http://www.ccp14.ac.uk/tutorial/tutorial.htm>.
- (10) DASH was written by W. I. F. David and K. Shankland and can be purchased from the Cambridge Crystallographic Data Centre, see www.ccdc.cam.ac.uk for more details.
- (11) David, W. I. F.; Shankland, K.; Shankland, N. *Chem. Commun.* **1998**, 931–932.
- (12) Pawley, G. S. *J. Appl. Crystallogr.* **1981**, *14*, 357–361.
- (13) LeBail, A.; Duroy, H.; Fourquet, J. L. *Mater. Res. Bull.* **1988**, *23*, 447–452.
- (14) Larson, A. C.; Von Dreele, R. B. GSAS Software Suite, LANSCE-Los Alamos National Laboratory, Los Alamos, NM.

(4) Cotton, F. A.; Extine, M.; Gage, L. D. *Inorg. Chem.* **1978**, *17*, 172–176.

(5) Martin, D. S.; Huang, H. W. *Inorg. Chem.* **1990**, *29*, 3674–3680.

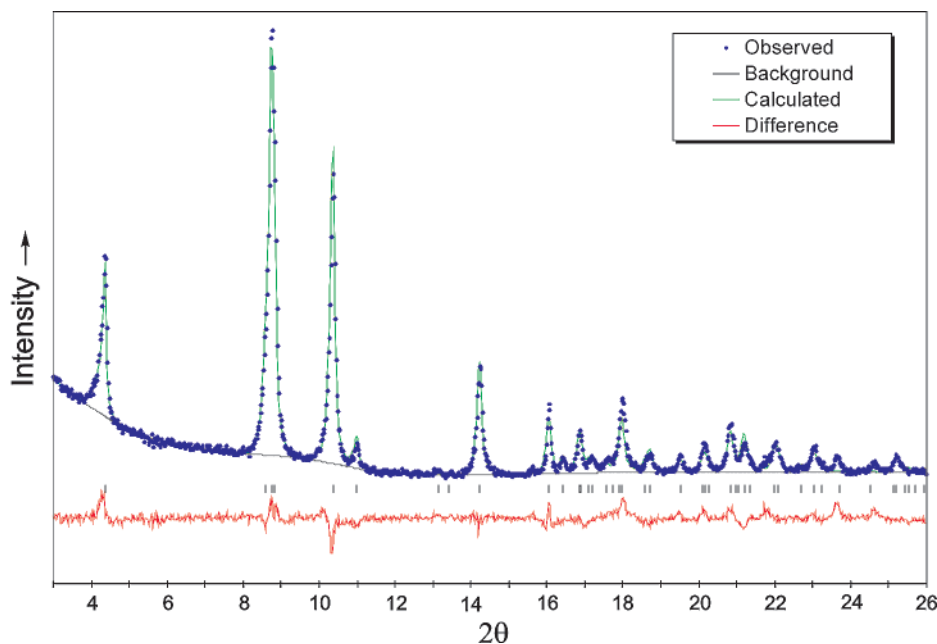


Figure 1. X-ray powder diffraction patterns for Mo₄PFT. The crosses represent the observed data points, while the solid line is the calculated fit to the diffraction pattern. The vertical lines at the bottom of the figure denote the expected peak positions.

Table 1. Crystallographic Data for [(^tBuCO₂)₃Mo₂(μ-O₂CC₆F₄CO₂)Mo₂(O₂C^tBu)₃]

parameter	value	parameter	value
formula	Mo ₄ C ₃₈ H ₅₄ F ₄ O ₁₆	<i>d</i> (calcd)/g cm ⁻³	1.681
FW/g mol ⁻¹	1226.6	2θ range/°	3–26
crystal system	monoclinic	temperature/K	295
space group	C2	wavelength/Å	1.5406
<i>a</i> /Å	21.002	<i>N</i> _{ref} ^a	45
<i>b</i> /Å	5.7219	<i>N</i> _{var} ^b	5
<i>c</i> /Å	20.562	χ ² (Pawley fit-DASH)	2.52
β/°	101.32	χ ² (solution-DASH)	5.82
volume/Å ³	2423	<i>R</i> _{wp} (Pawley fit-reflex)	0.0748
<i>Z</i>	2	<i>R</i> _{wp} (refinement-reflex)	0.0906

^a *N*_{ref} = number of reflections in the refined data range. ^b *N*_{var} = number of structural variables in the final rigid body refinement (defining the location and orientation of the molecule as well as the torsional degrees of freedom).

evaluated during the final stages of the refinement. The disordered model provided a fit (*R*_{wp} = 0.0796) to the experimental data that is far superior to models with the plane of the C₆F₄ ring either parallel (*R*_{wp} = 0.142) or perpendicular (*R*_{wp} = 0.113) to the 2-fold axis. Additionally, the model with the plane of the aromatic ring parallel to the 2-fold axis leads to unrealistically short (~1 Å) F⋯F contacts.

In the solid state, Mo₄PFT is a coordination polymer formed through the agency of M⋯O intermolecular bonds of the type shown in **I**. However, the dihedral angle between the two M–M axes is 54°, leading to a “twisted-staircase” structure. A space-filling molecular packing diagram and the intermolecular connectivity within the extended chain structure are shown in Figures 2 and 3, respectively. Also shown in Figure 3 is a view of the central (CO₂)₃Mo₂(μ-O₂CC₆F₄CO₂)Mo₂(O₂C)₃ skeleton viewed perpendicular to the C₂ axis. This shows how the two Mo₂ units are oriented with respect to each other and to the C₆F₄ ring. One of the Mo₂ units is almost coplanar with the C₆F₄ ring. This is pertinent to the electronic absorption spectra which are discussed later. Although the geometrical parameters associated with the central Mo₂O₈ core have not been refined from those of the input model, the present solution unequivocally

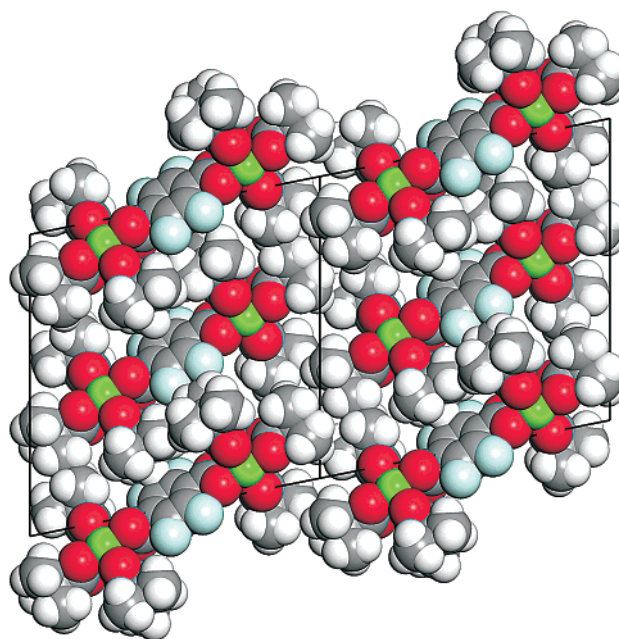


Figure 2. Space filling representations of the crystal packing in Mo₄PFT showing one layer of molecules viewed down the *b*-axis. Atomic color scheme: Mo = green, O = red, C = gray, F = light blue, and H = white.

defines the coordination features, molecular packing, and gross conformation of the solid-state structure of Mo₄PFT. Thus, the structure solution accurately represents the crystal packing of the molecule in the solid state but is not of sufficient resolution to define specific bond distances and angles within the molecule.

Bonding and Electronic Structure Calculations. When two M₂ units with quadruple bonds are united by a dicarboxylate bridge, O₂C–X–CO₂, the electronic communication between the M₂ centers is principally influenced by the dihedral angle between the two M₂O₂C planes, and the nature of X. When X is absent, the bridge is oxalate, and the electronic coupling of the M₂ centers arises from the in- and out-of-phase combination

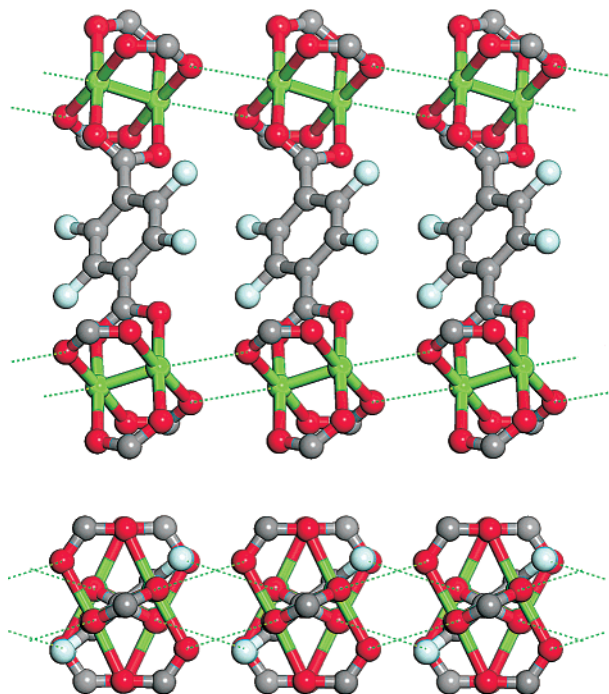
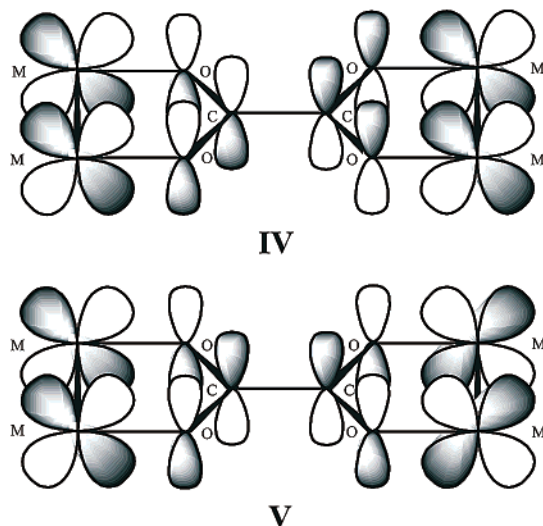


Figure 3. The intermolecular Mo–O interactions in Mo₄PFT which run parallel to the *b*-axis. The top drawing shows the two-dimensional infinite polymeric structure of Mo₄PFT, whereas the bottom drawing illustrates the relationship of the two Mo₂ units and the C₆F₄ ring. The atomic color scheme is as in Figure 2.

of the δ orbitals and their interactions with the filled and empty oxalate orbitals as shown in IV and V, respectively.



This orbital interaction is a maximum for planar D_{2h} oxalate and a minimum for the 90° twisted D_{2d} oxalate. The insertion of X between the two M_2O_2C units will mediate the electronic coupling. For example, if $X = (CH_2)_n$, the effect will be to insulate the two redox-active dimetal centers, but if $X = (C\equiv C)_n$ or $(CH=CH)_n$, the linking entity will serve as a carbon molecular wire. The $-C_6F_4-$ moiety falls within the latter class of bridges because the C_6 aromatic π system can interact with the two M_2O_2C δ - π combinations. Simple considerations lead to the expectation that the maximum coupling of the M_2 centers will occur for a planar D_{2h} structure. The key orbital interaction

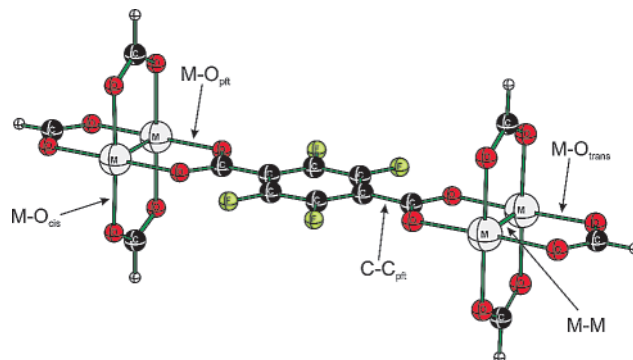
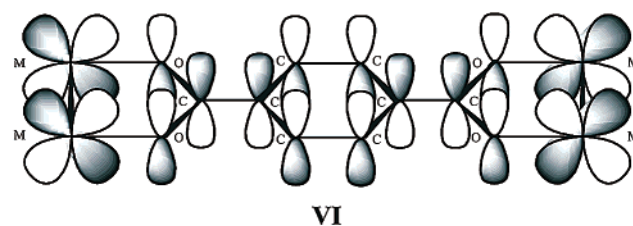


Figure 4. View of the fully relaxed $\theta = 0^\circ$ D_{2h} $(HCO_2)_3M_2(\mu-O_2CC_6F_4CO_2)M_2(O_2CH)_3$, where $M = Mo$ or W . Corresponding selected metrical data are given in Table 2.

involves the in-phase M_2 δ combination and the empty $O_2CC_6F_4CO_2$ π^* orbital as is shown schematically in VI.



To interrogate the electronic structure of the M_4 PFT complexes, we have carried out electronic structure calculations employing DFT on the model compounds $(HCO_2)_3M_2(\mu-O_2CC_6F_4CO_2)M_2(O_2CH)_3$, where $M = Mo$ or W , using both the Gaussian 98¹⁵ and the ADF 2000.01^{16–19} programs (see Experimental Section for details). Initially, calculations were performed under D_2 symmetry with a starting dihedral angle of 45° between the C_6F_4 ring and the M_2 vectors (90° between M_2 vectors). However, the optimized geometry was in all cases the planar D_{2h} structure shown in Figure 4. The electronic structures of the geometry-optimized D_{2h} models with the C_6F_4 planes at right angles to the M_2 vectors were also calculated. The energy difference between the two structures is small, ca. $2\text{--}3$ kcal mol⁻¹ for $M = Mo$ and $4\text{--}5$ kcal mol⁻¹ for $M = W$, and this can be taken as an estimate of the electronic barrier to phenyl group rotation. An orbital energy diagram of the frontier molecular orbitals of the D_{2h} $\theta = 0^\circ$ and the $\theta = 90^\circ$ structures for both $M = Mo$ and W is shown in Figure 5. Calculated structural data are given in Table 2.

For the ground-state structures, $\theta = 0^\circ$, the HOMO and HOMO–1 are the metal-based MOs with M_4 δ character, b_{2g}

- (15) Frisch, M. J.; Trucks, G. W.; Schlegel, H. B.; Scuseria, G. E.; Robb, M. A.; Cheeseman, J. R.; Zakrzewski, V. G.; Montgomery, J. A. J.; Stratmann, R. E.; Burant, J. C.; Dapprich, S.; Millam, J. M.; Daniels, A. D.; Kudin, K. N.; Strain, M. C.; Farkas, O.; Tomasi, J.; Barone, V.; Cossi, M.; Cammi, R.; Mennucci, B.; Pomelli, C.; Adamo, C.; Clifford, S.; Ochterski, J.; Petersson, G. A.; Ayala, P. Y.; Cui, Q.; Morokuma, K.; Malick, D. K.; Rabuck, A. D.; Raghavachari, K.; Foresman, J. B.; Cioslowski, J.; Ortiz, J. V.; Baboul, A. G.; Stefanov, B. B.; Liu, G.; Liashenko, A.; Piskorz, P.; Komaromi, I.; Gomperts, R. J.; Martin, R. L.; Fox, D. J.; Keith, T.; Al-Laham, M. A.; Peng, C. Y.; Nanayakkara, A.; Challacombe, M.; Gill, P. M. W.; Johnson, B.; Chen, W.; Wong, M. W.; Andres, J. L.; Gonzalez, C.; Head-Gordon, M.; Replogle, E. S.; Pople, J. A. *Gaussian 98*, revision A.9; Gaussian Inc.: Pittsburgh, PA, 1998.
- (16) Baerends, E. J.; Ellis, D. E.; Ros, P. *Chem. Phys.* **1973**, *2*, 41–51.
- (17) Verluis, L.; Ziegler, T. *J. Chem. Phys.* **1988**, *88*, 322–328.
- (18) te Velde, G.; Baerends, E. J. *J. Comput. Phys.* **1992**, *99*, 84–98.
- (19) Guerra, C. F.; Snijders, J. G.; te Velde, G.; Baerends, E. J. *Theor. Chem. Acc.* **1998**, *99*, 391–403.

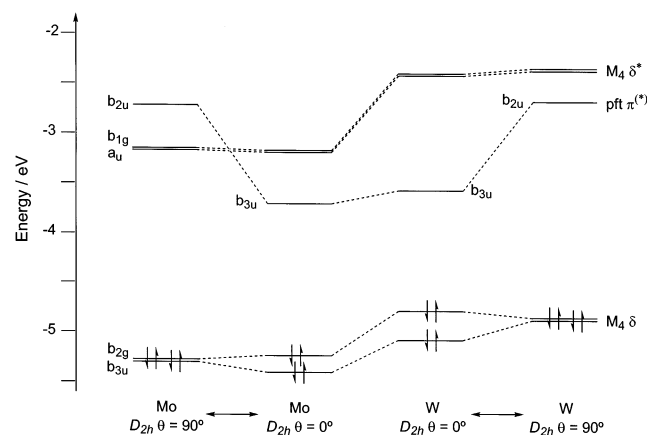


Figure 5. Comparative molecular orbital energy level diagram for $\theta = 0$ and 90° D_{2h} $(\text{HCO}_2)_3\text{M}_2(\mu\text{-O}_2\text{CC}_6\text{F}_4\text{CO}_2)\text{M}_2(\text{O}_2\text{CH})_3$, $\text{M} = \text{Mo}$ or W .

Table 2. Calculated Geometric Data for the D_{2h} 0° and D_{2h} 90° Forms of the Formate Models of M_4PFT from Gaussian and ADF (in Parentheses) Calculations, Respectively

	Mo D_{2h} $0^\circ/\text{\AA}$	Mo D_{2h} $90^\circ/\text{\AA}$	W D_{2h} $0^\circ/\text{\AA}$	W D_{2h} $90^\circ/\text{\AA}$
M–M	2.121 (2.146)	2.119 (2.144)	2.204 (2.233)	2.202 (2.230)
M–O _{pft}	2.095 (2.097)	2.120 (2.123)	2.074 (2.057)	2.108 (2.095)
M–O _{trans}	2.123 (2.098)	2.118 (2.107)	2.119 (2.097)	2.108 (2.084)
M–O _{cis}	2.121 (2.106)	2.120 (2.086)	2.112 (2.072)	2.110 (2.069)
C–C _{pft}	1.482 (1.479)	1.498 (1.499)	1.470 (1.459)	1.495 (1.494)

and b_{3u} , respectively. The energy separation is ca. 50% larger when $\text{M} = \text{W}$ than for $\text{M} = \text{Mo}$, and the orbital energies are higher for $\text{M} = \text{W}$, cf. M_4OXA .² The magnitude of the energy separation between the corresponding b_{2g} and b_{3u} orbitals is slightly smaller for the pft-bridged complexes than for the oxalate-bridged analogues. The LUMO is, for both $\text{M} = \text{Mo}$ and W , the bridge-based b_{3u} orbital, and slightly higher in energy are the a_u and b_{1g} $\text{M}_4 \delta^*$ orbitals.

In the other D_{2h} structure where $\theta = 90^\circ$, and the C_6F_4 ring is at right angles to the M_4 plane, the $\text{M}_4 \delta$ orbitals are almost isoenergetic. For $\text{M} = \text{Mo}$, the LUMO and LUMO+1 are the $\text{M}_4 \delta^*$ orbitals, but, for $\text{M} = \text{W}$, the LUMO is predicted to be the bridge-based MO of now b_{2u} symmetry. As can be seen from an inspection of Figure 5, the b_{nu} ($n = 2$ or 3) bridge-based orbital is, for both $\text{M} = \text{Mo}$ and W , very sensitive to the twist angle θ , and its energy changes by ca. 1 eV between $\theta = 0$ and 90° . The HOMO–LUMO gap for $\text{M} = \text{Mo}$ spans the range from 1.53 to 2.57 eV for $\theta = 0$ and 90° , respectively, but for $\text{M} = \text{W}$, the gap is smaller, spanning the range from 1.22 to 2.18 eV. Because the HOMO–LUMO electronic transition, b_{2g} to b_{nu} , is a fully allowed MLCT transition, we would expect to see a rather intense low energy band in the electronic spectra of M_4PFT which might show interesting thermochromism, vide infra.

GaussView representations for the frontier MOs of $(\text{HCO}_2)_3\text{-M}_2(\mu\text{-O}_2\text{CC}_6\text{F}_4\text{CO}_2)\text{M}_2(\text{O}_2\text{CH})_3$ are shown in Figure 6. For $\theta = 0^\circ$, the stabilized b_{3u} $\text{M}_2 \delta$ orbital is seen to have some of the bridge character predicted by the quinonoid description shown in VI. The HOMO is principally $\text{M}_2 \delta$ with only a small contribution from the carboxylate ligands, while the LUMO is almost wholly quinonoidal and bridge centered. In the D_{2h} $\theta = 90^\circ$ structure, the phenyl π orbitals do not interact with the $\text{M}_2 \delta$ orbitals.

Electronic Absorption Spectra. The compound Mo_4PFT is mustard yellow in the solid state but red/orange in solution.

This red shift of the spectrum from solid state to solution is in the opposite direction from that seen for Mo_4OXA .² The room-temperature spectra recorded as a Nujol mull and that obtained in 2-MeTHF are compared in Figure 7.

The compound W_4PFT is dark blue in the solid state and a paler and brighter blue in 2-MeTHF as a result of an intense broad absorption band at ca. 800 nm, $\epsilon \approx 30\,000 \text{ M}^{-1} \text{ cm}^{-1}$. The room-temperature spectra recorded as a Nujol mull and that obtained in 2-MeTHF are compared in Figure 8. Upon lowering the temperature, we found that the solution spectra show a significant red shift. Indeed, the intense color of W_4PFT fades as the region of maximum absorption shifts from the visible to the near-infrared. The spectra recorded in a 2-MeTHF glass at 80 K and in solution at 150 K are also shown in Figure 8.

Qualitative interpretation of these observations may be based on the electronic structure calculations for the model compounds under D_{2h} symmetry. First, the intense low energy absorptions are due to metal-to-bridge charge-transfer transitions. These occur at lower energy for the tungsten than for the molybdenum compound because the tungsten $\text{M}_4 \delta$ HOMO is ca. 0.5 eV above the energy of the molybdenum counterpart. Second, the thermochromism, whereby the lowest energy absorption shifts to longer wavelength with cooling, can reasonably be explained in terms of the preference for the planar D_{2h} structure ($\theta = 0^\circ$) at lower temperatures. Recall that the calculations predicted that the HOMO–LUMO gap decreases by ca. 1 eV upon rotation of the C_6F_4 group from $\theta = 90^\circ$ to $\theta = 0^\circ$. The HOMO–LUMO transition is fully allowed, irrespective of the twist of the C_6F_4 ring with respect to the M_2 axes. It should be noted that in our calculations we simplified the structures to those in which the two M_2 units are symmetry related and indeed coplanar under D_{2h} symmetry. In reality, rotations about the carboxylate carbon to C_6F_4 *ipso* carbon bonds will allow this short chain molecule to behave as three independent paddles spinning about an axis which passes through both of these bonds and the centers of the $\text{M}–\text{M}$ quadruple bonds. It is therefore to be expected that the electronic absorption spectrum obtained in solution at room temperature is very broad and sharpens considerably as the temperature is lowered to 80 K, at which temperature the planar D_{2h} structure better represents the species present in the glass (Figure 8). In the solid state, there is a 54° dihedral angle between the two M_2 units, and the C_6F_4 ring is disordered. As best as we can determine, this disorder would lead to at least two $\text{M}_4 \delta$ -to-bridge charge-transfer transitions at significantly different energies.

To gain more insight into the nature of the observed electronic spectral features, we have used time-dependent density functional theory, TDDFT, in calculating the vertical transition energies of $(\text{HCO}_2)_3\text{M}_2(\mu\text{-O}_2\text{CC}_6\text{F}_4\text{CO}_2)\text{M}_2(\text{O}_2\text{CH})_3$.^{20–24} Electronic transition energies for the lowest MLCT δ -to-bridge transition are listed in Table 3 for calculations performed on the D_{2h} structures where $\theta = 0$ and 90° , using both Gaussian

- (20) Gross, E. K. U.; Kohn, W. *Adv. Quantum Chem.* **1990**, *21*, 255–291.
- (21) Bauernschmitt, R.; Ahlrichs, R. *Chem. Phys. Lett.* **1996**, *256*, 454–464.
- (22) Stratmann, R. E.; Scuseria, G. E.; Frisch, M. J. *J. Chem. Phys.* **1998**, *109*, 8218–8224.
- (23) van Gisbergen, S. J. A.; Snijders, J. G.; Baerends, E. J. *Comput. Phys. Commun.* **1999**, *118*, 119–138.
- (24) Rosa, A.; Baerends, E. J.; van Gisbergen, S. J. A.; Lenthe, E. v.; Groeneveld, J. A.; Snijders, J. G. *J. Am. Chem. Soc.* **1999**, *121*, 10356–10365.

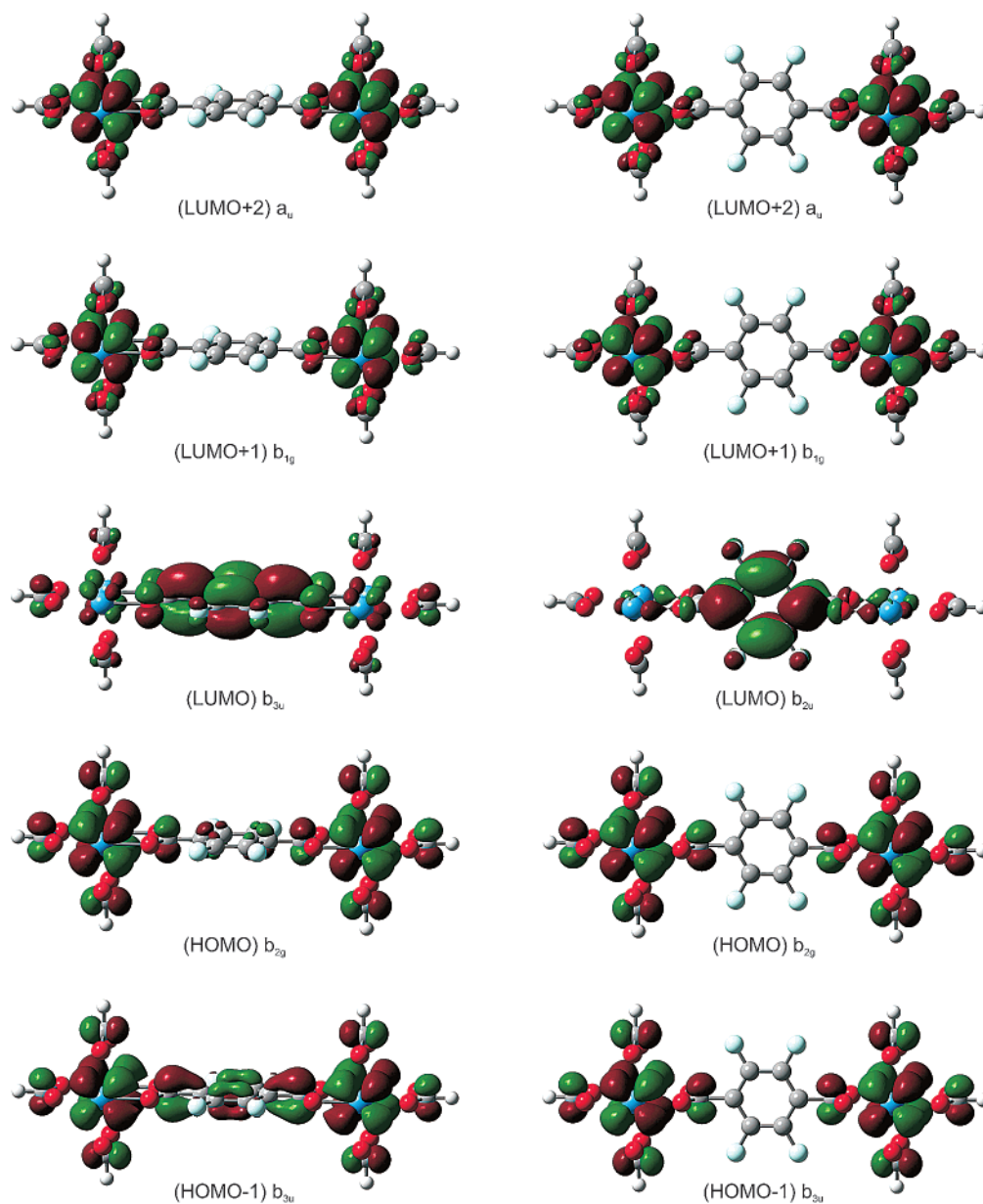


Figure 6. Molecular orbital plots for the frontier molecular orbitals of both $\theta = 0$ and 90° D_{2h} $(\text{HCO}_2)_3\text{W}_2(\mu\text{-O}_2\text{CC}_6\text{F}_4\text{CO}_2)\text{W}_2(\text{O}_2\text{CH})_3$.

98 and ADF 2000, along with the λ_{max} data observed for the M_4PFT complexes in THF solution at room temperature.³ As seen before for M_4OXA , the trends in energies are reproduced.² The observed transition energies are notably lower than the calculated values for tungsten, and this in part surely reflects the fact that spin-orbit coupling was not able to be included in the calculations. There are some other significant features in the mull spectra of W_4PFT and in the low-temperature spectra recorded as a glass that are not accounted for in this simple description. We shall focus on these and the emission spectra of the M_4PFT compounds in future work.

Raman and Resonance Raman Spectra. The Raman and resonance Raman spectra of the oxalate-bridged compounds M_4OXA are dominated by bands arising from the bridging oxalate ligand.² We therefore first recorded the Raman spectrum of perfluoroterephthalic acid, $p\text{-HO}_2\text{CC}_6\text{F}_4\text{CO}_2\text{H}$, H_2pft , to provide a guide to the wavenumbers of the bands of the perfluoroterephthalate bridging ligand.

H_2pft . The Raman spectrum of perfluoroterephthalic acid recorded with 647.1 nm excitation is shown in Figure 9, and the band maxima and possible assignments are given in Table 4. These assignments for the carboxylic acid modes and for the ring vibrations are guided partly by those published for the observed Raman bands of terephthalic acid ($p\text{-HO}_2\text{CC}_6\text{H}_4\text{CO}_2\text{H}$)²⁵ and 1,2,4,5-tetrafluorobenzene ($p\text{-C}_6\text{H}_2\text{F}_4$),²⁶ the wavenumbers of the key bands of each being included in Table 4. The skeletal modes are, of course, likely to be extensively coupled in H_2pft . The assignments of the 508 and 713 cm^{-1} bands of H_2pft to $\delta_s(\text{CO}_2)$ and ring breathing, respectively, must be considered tentative. The totally symmetric phenyl ring-breathing mode of benzene (mode 1 in Wilson's notation²⁷) occurs at 993 cm^{-1} but is coupled strongly with the totally

(25) Colombo, L.; Volovsek, V.; Furic, K.; Durig, J. R. *J. Raman Spectrosc.* **1990**, *21*, 169–175.

(26) Green, J. H. S.; Harrison, D. J. *Spectrochim. Acta* **1976**, *32A*, 1185–1193.

(27) Wilson, E. B. *Phys. Rev.* **1934**, *45*, 706.

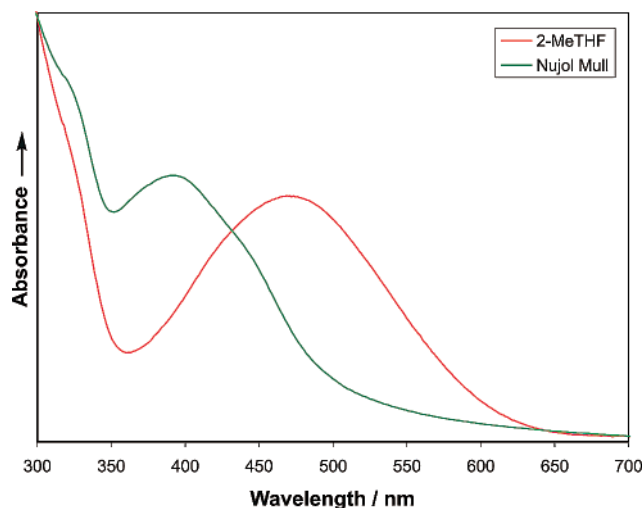


Figure 7. Electronic absorption spectra of Mo₄PFT as a 2-methyltetrahydrofuran solution and a Nujol mull both at 300 K.

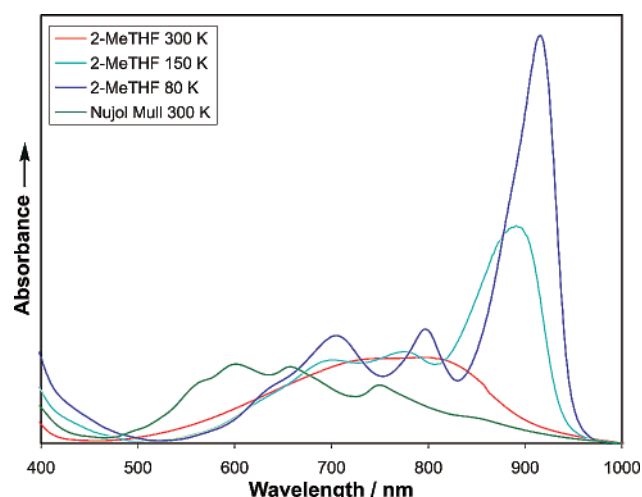


Figure 8. Electronic absorption spectra of W₄PFT as a 2-methyltetrahydrofuran solution at 300 and 150 K, a 2-methyltetrahydrofuran glass at 80 K, and a Nujol mull at 300 K.

symmetric C–X stretch in any substituted benzene, leading to wide variations in its wavenumber. The strong band of *p*-C₆H₂F₄ at 749 cm⁻¹ is assigned to this mode, so the medium band of H₂pft at 713 cm⁻¹ is so attributed. However, on intensity grounds, the strong band at 508 cm⁻¹ might alternatively be attributed to the ring-breathing mode, and the band at 713 cm⁻¹ to $\nu_s(\text{CO}_2)$, a value that is closer to that for *p*-HO₂CC₆H₄CO₂H (818 cm⁻¹).²⁵

Solid W₄PFT. The Raman spectrum of W₄PFT recorded with two different excitation wavelengths is shown in Figure 10, the band wavenumbers and possible assignments being given in Table 5. The spectrum of W₄PFT (Figure 10) is very similar to that of H₂pft; that is, it is dominated by bands of the bridging ligand, as found for the oxalate bridge of the analogous M₄OXA compounds.² This similarity allows for the ready identification of the band at 313 cm⁻¹ as being due to the WW stretch, that at 631 cm⁻¹ as being due to $\delta_s(\text{CO}_2)$ (piv), and the overlapping pair of bands at 1391 and 1409 cm⁻¹ as being due to $\nu_s(\text{CO}_2)$ (piv). The wavenumber of $\nu(\text{WW})$ is very close to those seen for W₂(O₂C'Bu)₄ (318 cm⁻¹)² and W₄OXA (311 cm⁻¹),² the wavenumber of $\delta_s(\text{CO}_2)$ (piv) is close to those of W₂(O₂C'Bu)₄ (629 and 635 cm⁻¹),² and the wavenumber of $\nu_s(\text{CO}_2)$ (piv) is

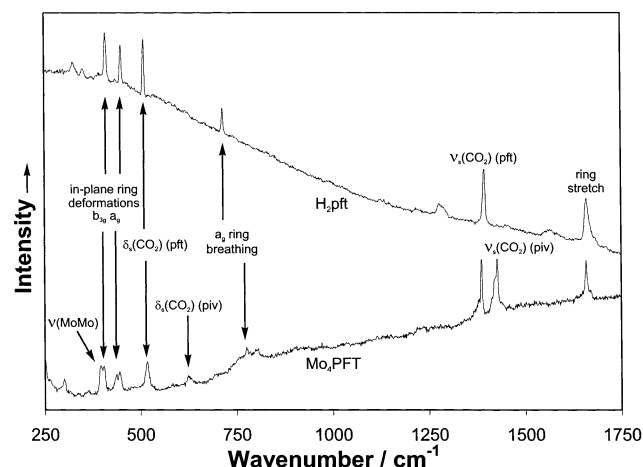
close to those of W₂(O₂C'Bu)₄ (1406 and 1413 cm⁻¹).² The band attributed to $\nu_s(\text{CO}_2)$ of the pft bridge falls 104 cm⁻¹ from 1392 to 1288 cm⁻¹ on coordination to W, whereas that for the analogous band of oxalate falls 126 cm⁻¹ on coordination to W in W₄OXA. The assignment of the strong band at 1603 cm⁻¹ is unclear: such a strong band is most likely to be fundamental, and the only reasonable assignment would seem to be $\nu_{as}(\text{CO}_2)$ (pft); however, it was not seen at all in the spectra of H₂pft or Mo₄PFT (see later). Another possible assignment is to the combination $\nu(\text{WW}) + \nu_s(\text{CO}_2)$ (pft) = 1601 cm⁻¹. The appearance of this band in the spectrum of W₄PFT could then be attributed to resonance effects (see below), although it is also seen in the off-resonance spectra. Both assignments are given in Table 5.

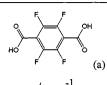
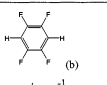
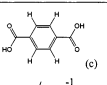
As is evident from Figure 10, the Raman spectra of W₄PFT depend on the wavelength of the laser lines used. The bands attributed to $\nu(\text{WW})$, $\delta_s(\text{CO}_2)$ (pft), and $\nu_s(\text{CO}_2)$ (pft) all increase in relative intensity, and the overtone band $2\delta_s(\text{CO}_2)$ is also seen on excitation at longer wavelength. After the intensity corrections were performed as described in the Experimental Section, the ratio of the band areas of the fundamentals to that of the reference band at 1392 cm⁻¹, attributed to $\nu_s(\text{CO}_2)$ (piv), is plotted in Figure S3 (Supporting Information), together with the electronic spectrum of solid W₄PFT recorded as a Nujol mull at 80 K. The Raman band at 1288 cm⁻¹, attributed to $\nu_s(\text{CO}_2)$ (pft), is enhanced upon excitation into the profile of this electronic band, but to a much lesser extent than that found for the analogous band $\nu_s(\text{CO}_2)$ (ox) in the resonance Raman spectra of M₄OXA.² However, for W₄PFT, the bands at 313 and 518 cm⁻¹ are enhanced to a greater extent than the 1288 cm⁻¹ band, analogous features not being seen in the spectra of M₄OXA. With the preferred assignment of the band at 518 cm⁻¹ as $\delta_s(\text{CO}_2)$ (pft), the enhancements in relative intensity can be interpreted as arising from a localized change in geometry of the W₂O₂C ring, consistent with a W₂ $\delta \rightarrow \text{CO}_2(\text{pft})$ b_{3u}(π) transition to the LUMO shown schematically in VI.

Solid Mo₄PFT. The Raman spectrum of Mo₄PFT, recorded with 647.1 nm excitation, is shown in Figure 9, and the band maxima and possible assignments are given in Table 5. As is the case for W₄PFT, the spectrum is very similar to that of H₂pft, and this similarity allows the band at 399 cm⁻¹ to be assigned to the MoMo stretch, the band at 626 cm⁻¹ to $\delta_s(\text{CO}_2)$ (piv), and the overlapping pair of bands at 1422 and 1427 cm⁻¹ to $\nu_s(\text{CO}_2)$ (piv). The wavenumber of $\nu(\text{MoMo})$ in Mo₄PFT is very close to those seen for Mo₂(O₂C'Bu)₄ (403 cm⁻¹)² and Mo₄OXA (395 cm⁻¹),² the wavenumber of $\delta_s(\text{CO}_2)$ (piv) is close to those of Mo₂(O₂C'Bu)₄ (624 and 632 cm⁻¹)² and Mo₄OXA (632 and 671 cm⁻¹)², and the wavenumber of $\nu_s(\text{CO}_2)$ (piv) is close to those found for Mo₂(O₂C'Bu)₄ (1416 and 1426 cm⁻¹)² and Mo₄OXA (1425 cm⁻¹).² The band attributed to $\nu_s(\text{CO}_2)$ of the bridging ligand is seen at 1386 cm⁻¹, 98 cm⁻¹ higher than that of W₄OXA. A similar difference (92 cm⁻¹) is seen between the analogous band wavenumbers of Mo₄OXA and W₄OXA. The uncertainty in the assignments of the bands seen at 519 and 781 cm⁻¹ follows from the discussion of the analogous bands in the spectra of H₂pft and W₄PFT. The electronic spectrum of solid Mo₄PFT shows a band centered at ca. 410 nm, and so Raman spectra of Mo₄PFT recorded with 568.2, 514.5, and 488.0 nm excitation would not be expected to display significant resonance enhancement. In practice, no extra bands

Table 3. Comparison of the Calculated Lowest δ -to-Perfluoroterephthalate- π^* Transition Energies Determined by TDDFT for the Formate Models of M_4 PFT by Gaussian and ADF (in Parentheses), and the Experimentally Observed Values for M_4 PFT in THF Solution at Room Temperature

wavelength	calculated excitation wavelength/nm	calculated excitation energy/eV	calculated oscillator strength (f)	obsd λ_{\max} THF/nm	obsd energy THF/eV	obsd ϵ THF/M $^{-1}$ cm $^{-1}$
Mo D_{2h} 0°	524(666)	2.37(1.86)	0.699(0.653)	470	2.64	10 500
Mo D_{2h} 90°	314(356)	3.95(3.48)	0.488(0.417)			
W D_{2h} 0°	610(707)	2.03(1.75)	1.000(1.047)	816	1.52	27 000
W D_{2h} 90°	356(393)	3.48(3.15)	0.633(0.513)			

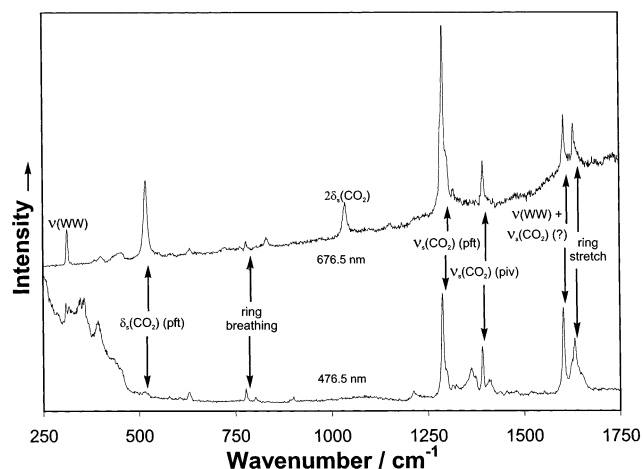
**Figure 9.** Raman spectra of H_2pft as a 50% KBr disk, and Mo_4PFT as the pure crystalline solid within a capillary, both at ca. 80 K, with 647.1 nm excitation and spectral slit widths of 4 cm^{-1} .**Table 4.** Wavenumbers and Assignments for the Raman Bands of H_2pft and Key Bands in the Raman Spectra of Terephthalic Acid and 1,2,4,5-Tetrafluorobenzene

			Assignment ^d
ν / cm^{-1}	ν / cm^{-1}	ν / cm^{-1}	
324 w	295 vs	625 w	out-of-plane ring def. (4, b_{2g})
349 w	—	286 m	$\rho_s(CO_2)$
409 s	422 vvs	632 vs	in-plane ring def. (6b, b_{3g})
449 s	488 s	260 s	in-plane ring def. (6a, a_g)
508 s	—	818 w	$\delta_s(CO_2)$
713 m	749 vvs	834 vs	ring breathing (1, a_g)
1274 w, br	—	—	—
1392 s	—	1308 vs	$\nu_s(CO_2)$
1449 w, br	—	1462 vs	$\delta(OH)$
1554 w, br	1369 s	—	$\nu_s(CF)$ (7a, a_g)
1659 s	1647 w	1612 s	in-plane ring stretch (8a, a_g)

^a H_2pft as a 50% KBr disk at ca. 80 K, $\lambda_0 = 647.1$ nm. ^b From ref 26; solid, neither temperature nor excitation wavelength reported. ^c From ref 25; powder, 20 K, $\lambda_0 = 514.5$ nm. ^d Numbers in parentheses are Wilson's notation for phenyl ring vibrations. The symmetry of each mode for the point group D_{2h} is also indicated.

or changes in relative band intensities were seen on change of excitation line wavelengths.

Mo_4PFT in THF. Mo_4PFT is readily soluble in THF, the mustard yellow powder giving a deep red/orange solution. The emission spectrum of the solid as a Nujol mull shows a band maximum at ca. 400 nm, which red shifts to 470 nm in THF solution, both being at room temperature (Figure 7). An attempt was therefore made to record an off-resonance spectrum using 647.1 nm excitation, but the resulting spectrum consisted of only weak Raman bands on an intense emission background. The profile of this emission was recorded by exciting the sample with 488.0 nm radiation and scanning the monochromator out to ca. 700 nm. After correcting for the wavelength-dependent throughput of the monochromator, we obtained the emission

**Figure 10.** Raman spectra of W_4PFT as the pure crystalline solid within a capillary at ca. 80 K, with 476.5 and 676.5 nm excitations and spectral slit widths of 4 cm^{-1} .

spectrum shown in Figure 11. Note that Raman bands appear in this spectrum between 520 and 535 nm. The absorption spectrum of Mo_4PFT in solution (Figure 11) is a mirror image of the emission spectrum, the crossing point of the two spectra (574 nm, 17 400 cm^{-1}) being a good estimate of the wavenumber of the vibronic 0–0 band. The Raman spectrum of Mo_4PFT in THF was recorded with excitation wavelengths ranging from 647.1 to 457.9 nm. That recorded with 457.9 nm excitation is shown in Figure 12, the band maxima being reported in Table 6, along with those of solid Mo_4PFT for comparison. In the region of the fundamentals below 1700 cm^{-1} , the two spectra are very similar. The wavenumber of $\nu(MoMo)$ is unchanged on going from the solid to solution. The wavenumber of the totally symmetric phenyl ring-breathing mode (mode 1 in Wilson's notation) increases by 1 cm^{-1} , while those of the other bands decrease by between 1 and 17 cm^{-1} on going from the solid to the solution. The largest decrease in wavenumber, ca. 20 cm^{-1} , occurs for $\nu_s(CO_2)$ (piv). These small changes may be attributed to the structure change on going from solid to solution and to the different temperatures at which the two sets of measurements were performed, viz., 80 K for the solid and room temperature for the solution spectra. The assignments of the bands seen in the solution spectrum at 518 and 782 cm^{-1} to $\delta_s(CO_2)$ (pft) and the ring-breathing mode 1, respectively, are tentative and could possibly be interchanged (see above).

The Raman spectrum of Mo_4PFT with 457.9 nm excitation (Figure 12) is really a resonance Raman spectrum because this line falls within the contour of an electronic absorption band. This is made manifest by the appearance of the combination bands above 1700 cm^{-1} not seen with any of the other excitation lines used. There are also small changes in the relative intensities of some of the bands as a function of excitation wavelength.

Table 5. Wavenumbers and Assignments for the Raman Bands of H₂pft and Mo₄PFT and W₄PFT^a

H ₂ pft 647.1 nm ν/cm^{-1}	Mo ₄ PFT 647.1 nm ν/cm^{-1}	W ₄ PFT 476.5 nm ν/cm^{-1}	W ₄ PFT 676.5 nm ν/cm^{-1}	assignment ^b
			204 w	
	304 w			$\nu(\text{MoO})$
	341 vw			$\nu(\text{MoO})$
	367 vw			$\nu(\text{MoO})$
324 w				out-of-plane ring def. (4, b _{2g})
349 w				$\rho_r(\text{CO}_2)$
	399 m	313 w	313 m	$\nu(\text{MM})$
			384 vw	
409 s	409 m		400 w	in-plane ring def. (6b, b _{3g})
449 s	441 m		447 w, br	in-plane ring def. (6a, a _g)
	453 m			$\rho_r(\text{CO}_2)(\text{piv})$
508 s	519 m	516 w	518 ms	$\delta_s(\text{CO}_2)(\text{pft})$
	626 w	631 w	631 w	$\delta_s(\text{CO}_2)(\text{piv})$
			723 vw	
713 m	781 w	779 m	777 w	ring breathing (1, a _g)
	804 w	804 w		
			832 w	$\nu(\text{WW}) + \delta_s(\text{CO}_2)(\text{pft})$
		902 w		$\nu(\text{C}-\text{CMe}_3)$
			1035 m	$2\delta_s(\text{CO}_2)(\text{pft})$
			1150 w	
		1213 m		$\nu(\text{C}-\text{Me}_3)$
1274 w, br				
1392 s	1386 s	1288 vs	1288 s	$\nu_s(\text{CO}_2)(\text{pft})$
		1299 sh	1298 sh	$\delta_s(\text{CO}_2)(\text{pft}) + \text{ring breathing}$
		1314 w	1315 w	$\delta_s(\text{CO}_2)(\text{pft}) + 804$
		1323 w		
		1362 m		$\delta_s(\text{CH}_3)$
	1422 sh	1391 s	1392 m	$\nu_s(\text{CO}_2)(\text{piv})$
	1427 s	1409 m		$\nu_s(\text{CO}_2)(\text{piv})$
		1437 w		$\delta_{\text{as}}(\text{CH}_3)$
		1454 w		$\delta_{\text{as}}(\text{CH}_3)$
		1478 w		$\delta_{\text{as}}(\text{CH}_3)$
1449 w, br				$\delta(\text{OH})$
1554 w, br		1522 vw		$\nu_s(\text{CF})(7a, a_g)$
		1603 vs	1603 m	$\nu_{\text{as}}(\text{CO}_2)(\text{pft})$ or $\nu(\text{WW}) + \nu_s(\text{CO}_2)(\text{pft})$
1659 s	1659 s	1632 s	1628 m	in-plane ring stretch (8a, a _g)
		1804 w	1801 w, br	$\delta_s(\text{CO}_2)(\text{pft}) + \nu_s(\text{CO}_2)(\text{pft})$
		2567 ms		$2\nu_s(\text{CO}_2)(\text{pft})$
		2676 s		$\nu_s(\text{CO}_2)(\text{pft}) + \nu_s(\text{CO}_2)(\text{piv})$
		2888 ms	obscured by fluorescence as shown in Table 5	$\nu_s(\text{CO}_2)(\text{pft}) + 1603$
		2916 m		$\nu_s(\text{CO}_2)(\text{pft}) + 8a$
		3232 s		$1603 + 8a$

^a H₂pft as a 50% KBr disk, and Mo₄PFT and W₄PFT as the pure crystalline solids within capillaries, all at ca. 80 K. ^b Numbers in parentheses are Wilson's notation for phenyl ring vibrations. The symmetry of each mode for the point group D_{2h} is also indicated.

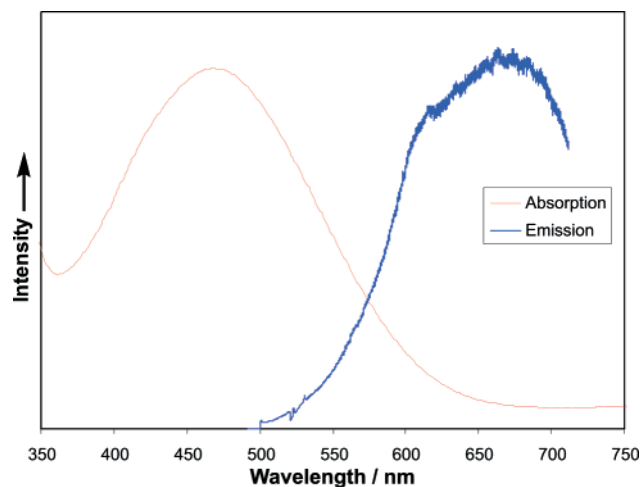


Figure 11. Emission spectrum of Mo₄PFT at 300 K in tetrahydrofuran measured using 488.0 nm excitation, along with the electronic spectrum of the complex also recorded at 300 K.

The band used as the intensity reference for determining the excitation profiles of bands of solid W₄PFT is here seen at 1405 cm^{-1} , overlapping the strong band at 1378 cm^{-1} and making

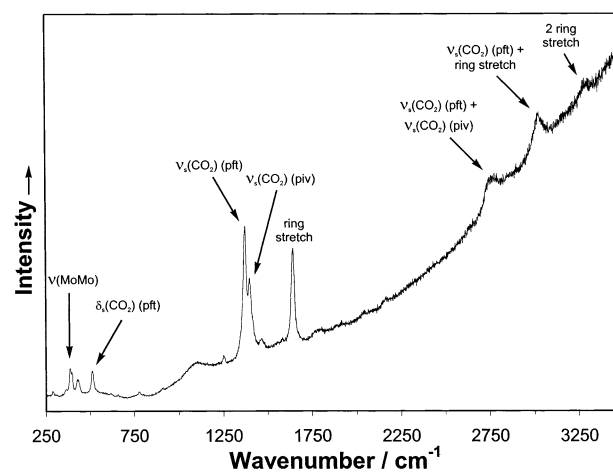


Figure 12. Resonance Raman spectrum of Mo₄PFT as a tetrahydrofuran solution sealed within a capillary at 300 K, with 457.9 nm excitation and spectral slit width of 3 cm^{-1} .

intensity measurements on either unreliable. After correcting the spectral intensities as described above, we determined the band intensities relative to that of the band at 1649 cm^{-1} , chosen

Table 6. Wavenumbers and Assignments for the Raman Bands of Mo₄PFT as the Solid and in Tetrahydrofuran Solution^a

solid Mo ₄ PFT ν/cm^{-1}	Mo ₄ PFT in THF ν/cm^{-1}	assignment ^b
	194 w	
	250 w	
304 w	294 w	$\nu(\text{MoO})$
341 w		$\nu(\text{MoO})$
367 w		$\nu(\text{MoO})$
399 m	399 m	$\nu(\text{MoMo})$
409 m		in-plane ring def. (6b, b _{3g})
441 m	436 m	in-plane ring def. (6a, a _g)
453 m		$\rho_r(\text{CO}_2)$ (piv)
519 m	518 m	$\delta_s(\text{CO}_2)$ (pft)
626 w	621 vw	$\delta_s(\text{CO}_2)$ (piv)
	663 vw	
781 w	782 w	ring breathing (1, a _g)
	1257 wm	
1386 s	1378 vs	$\nu_s(\text{CO}_2)$ (pft)
1422 sh	1405 s	$\nu_s(\text{CO}_2)$ (piv)
1427 s		$\nu_s(\text{CO}_2)$ (piv)
	1474 m	$\delta_{\text{as}}(\text{CH}_3)$
1659 s	1649 s	in-plane ring stretch (8a, a _g)
	1797 m, br	$\nu(\text{MoMo}) + \nu_s(\text{CO}_2)$ (piv)
	2048 w	$\nu(\text{MoMo}) + 8a$
	2173 w	1 + $\nu_s(\text{CO}_2)$ (piv) (?)
	2774 m, br	$\nu_s(\text{CO}_2)$ (pft) + $\nu_s(\text{CO}_2)$ (piv)
	3037 m, br	$\nu_s(\text{CO}_2)$ (pft) + 8a
	3294 m, br	2 (8a)

^a Solid Mo₄PFT as the pure crystalline solid within a capillary, at ca. 80 K, $\lambda_0 = 647.1$ nm. Mo₄PFT in tetrahydrofuran within a capillary, at room temperature, $\lambda_0 = 457.9$ nm; no bands arising from tetrahydrofuran could be detected owing to the resonance enhancement to the Raman active bands of Mo₄PFT. ^b Numbers in parentheses are Wilson's notation for phenyl ring vibrations. The symmetry of certain modes for the point group D_{2h} is also indicated.

as the internal reference because it is strong, sharp, and isolated. This is not a completely satisfactory way of defining the excitation profiles of the other bands because of possible variations in the relative intensity of the band (see Table 6). The excitation profiles of the bands at 399, 436, and 518 cm^{-1} are shown in Figure S4 (Supporting Information), which reveal that the relative intensity of the $\nu(\text{MoMo})$ band at 399 cm^{-1} increases on excitation into the electronic band centered at 470 nm, while those of the other two bands increase to a much lesser extent. The resonance enhancement of $\nu(\text{MoMo})$ is consistent with excitation at resonance with the Mo₂ δ to δ^* electronic transition expected in the 400–500 nm range. The relative intensity of the band at 1378 cm^{-1} , assigned to $\nu_s(\text{CO}_2)$ (pft), surprisingly stays constant over the range of excitation wavelengths used here. From the electronic spectrum of Mo₄PFT in THF (Figure 11), it is clear that these excitation profiles do not follow the profile of the electronic band at 470 nm. The preferred assignment of the 518 cm^{-1} band is to $\delta_s(\text{CO}_2)$ (pft), the excitation profiles being consistent with a change in geometry of the Mo₂O₂C ring upon electronic excitation; in addition, changes to the C₆F₄ ring geometry take place, as revealed by the enhancement of the in-plane C₆F₄ ring deformation mode 6a and the involvement of the ring-stretching mode 8a in various combination bands. This involvement of the ring-stretching mode is completely consistent with the quinonoidal form of the b_{3u} LUMO.

The three samples studied here have shown different Raman spectral behavior on excitation into their electronic transitions. For solid W₄PFT, the band attributed to $\delta_s(\text{CO}_2)$ (pft) and its first overtone show greatest enhancement, with those attributed

to $\nu_s(\text{CO}_2)$ (pft) and $\nu(\text{WW})$ being enhanced to lesser extents. For solid Mo₄PFT, there is no evidence for resonance enhancement upon excitation into the profile of the electronic transition, while for Mo₄PFT in THF, the greatest enhancement is for the band attributed to $\nu(\text{MoMo})$, with those attributed to the ring deformation mode 6a and $\delta_s(\text{CO}_2)$ (piv) being enhanced to lesser extents. The ring-stretching mode 8a is also seen in combinations. The enhancement of the bands in the spectrum of solid W₄PFT is consistent with a change in the geometry of the W₂O₂C ring on electronic excitation, which is in turn consistent with excitation into the LUMO. For Mo₄PFT in THF, the resonance Raman spectrum shows that there is a change both in the geometry of the Mo₂O₂C ring and also in the C₆F₄ ring on electronic excitation. This is consistent with electronic excitation into the LUMO, but with larger contributions from the C₆ π orbitals than is the case for the analogous LUMO in W₄PFT. For solid Mo₄PFT, no resonance enhancement is seen, presumably because the resonant electronic transition at ca. 410 nm is too distant from the nearest laser wavelength (457.9 nm) available.

The resonance behavior of the Raman spectra of M₄PFT can be compared to that of the M₄OXA compounds, where strong enhancement of $\nu_s(\text{CO}_2)$ (ox) is seen for both M = W and Mo. These enhancements are consistent with changes in geometry of the M₂O₂C rings and with the assignment of the electronic bands to M₂ $\delta \rightarrow \text{CO}_2$ (ox) π^* transitions. For the M₄PFT complexes, the analogous electronic transitions are to a LUMO which also includes contributions from π orbitals on the C₆F₄ ring, and hence the geometric change on electronic excitation involves both the phenyl and the M₂O₂C rings, with a greater change in the C₆F₄ ring geometry in the case of Mo₄PFT in THF than for solid W₄PFT.

Concluding Remarks

The electronic structure calculations on the model compounds [(HCO₂)₃M₂(μ -O₂CC₆F₄CO₂)M₂(O₂CH)₃] have provided insight into the interesting color changes of solid state and solution samples of M₄PFT compounds. This solvatochromism and the observed solution thermochromism are related to the degree of M₂ δ to bridge π^* orbital mixing, which is at a maximum for the planar D_{2h} form of the molecule. These effects also have consequences in the Raman spectra of the compounds. This work also provides an example of the application of XPRD in the determination of the molecular packing in the solid state in the absence of single crystals suitable for the now routine single-crystal X-ray determination of structure.

Finally, we note that, on the basis of this work, we anticipate interesting thermochromism for so-called molecular squares having a central [M₂(μ -O₂CC₆F₄CO₂)]₄ core in which the M₂ units possess quadruple bonds. Moreover, the orientation of the C₆F₄ rings will be influenced by the presence of solvent or guest molecules occupying a position within the open box. This can be expected to give rise to solvent or guest optical signatures.

Experimental Section

Because of the air-sensitive nature of the complexes, all were synthesized and manipulated under dinitrogen or argon atmospheres using either standard Schlenk-line or drybox techniques. The preparation of the M₄PFT compounds followed previously described procedures.³ Toluene and hexane were predried over activated molecular sieves and refluxed over molten sodium and potassium, respectively, under an

atmosphere of dinitrogen, collected by distillation, and then degassed. Samples of the complexes were stored in sealed ampules or capillaries in a dinitrogen-filled drybox.

Powder X-ray Diffraction and Structure Solution. Powder samples of Mo_4PFT were ground using a pestle and mortar and then sealed in 0.7 mm diameter glass capillaries (W. Müller). X-ray powder diffraction patterns were collected in-house using a Bruker D8 diffractometer equipped with a sealed copper X-ray tube, an incident beam Ge (111) monochromator, a spinning capillary sample stage, and a scintillation detector. The data were collected by step scanning over the angular range $3^\circ < 2\theta < 26^\circ$ using a step size of 0.02° in 2θ .

Molecular and Electronic Structure Calculations. Molecular and electronic structure determinations on the model compounds $(\text{HCO}_2)_3\text{-M}_2(\mu\text{-O}_2\text{CC}_6\text{F}_4\text{CO}_2)\text{M}_2(\text{O}_2\text{CH})_3$ were performed using DFT with both the Gaussian 98¹⁵ and the ADF 2000.01^{16–19} programs. In Gaussian 98, the B3LYP^{28–30} functional was used, along with the 6-31G* (5d) basis set for H, C, O, and F,³¹ and the SDD energy consistent pseudopotentials for Mo and W.³² In ADF 2000, the exchange and correlation functionals of Perdew and Wang^{33,34} were used, along with a double- ζ Slater basis set with d-type polarization functions for H, C, O, and F (1s frozen core for C and O), and triple- ζ basis sets were employed for both Mo (3d frozen core) and W (4d frozen core). ZORA scalar relativistic corrections were applied to both Mo and W systems under ADF.^{35–39} All geometries were fully optimized at the above levels using the default optimization criteria of the respective programs. Orbital analyses were completed with GaussView.⁴⁰ Electronic absorption spectra were predicted using the TDDFT method implemented within the Gaussian 98 and ADF 2000.01 programs, and using the default optimization criteria.^{20–24}

Variable Temperature Electronic Absorption Spectra. Spectra were obtained using an Oxford Instruments OptistatBath helium cryostat placed within the sample compartment of either a Perkin-Elmer Lambda 19 UV–vis–NIR absorption spectrometer or a Perkin-Elmer Lambda

900 UV–vis–NIR absorption spectrometer. Samples were prepared in an inert atmosphere drybox and injected into either a 150 μL copper cell consisting of two quartz windows separated by a permeable synthetic rubber spacer or standard Quartz 10 mm path-length cuvettes. Spectra of the compounds in the solution state were obtained in thoroughly degassed optical quality anhydrous 2-methyltetrahydrofuran (2-MeTHF, Aldrich), which forms a glass at ca. 130–40 K, while spectra of the compounds in the solid state were obtained as Nujol (Wilmad) mulls. All spectra were cumulatively averaged from 2 to 3 scans taken with a scan rate of 120 nm min^{-1} and using a 1–2 nm band-pass.

Raman and Resonance Raman Spectra. Raman spectra of solid W_4PFT and Mo_4PFT were recorded on samples sealed into capillary tubes held in a cryostat and cooled with liquid nitrogen. Spectra were recorded after excitation with a range of lines from Coherent I70 Ar^+ and I301 Kr^+ lasers, between 488.0 and 647.1 nm for Mo_4PFT and 457.9 and 676.5 nm for W_4PFT . These compounds showed degradation upon intense laser irradiation, so in all cases the spectra were recorded with powers at the sample of less than 10 mW. Raman spectra were recorded from Mo_4PFT solutions in capillaries held across the exciting laser beam at room temperature. Solutions were excited with lines of wavelengths between 647.1 and 457.9 nm, with the laser power kept below 30 mW for all excitation wavelengths. Scattered radiation was dispersed through a Spex 1401 double monochromator, with entrance and exit slits set to correspond to a spectral resolution of 4 cm^{-1} for solid samples and 3 cm^{-1} for the solutions, and detected with a Burle C31034-02 photomultiplier tube. Wavenumber calibration was achieved by superimposing neon emission lines on the recorded spectra to give an estimated accuracy of $\pm 1 \text{ cm}^{-1}$. Spectral intensities were corrected for the wavelength dependence of the spectrometer throughput and the ν^4 dependence of the scattering efficiency, and band areas were measured by fitting Lorentzian functions to the observed band profiles. The spectrum of $p\text{-HO}_2\text{CC}_6\text{F}_4\text{CO}_2\text{H}$ was recorded as an ca. 50:50 disk with KBr at liquid nitrogen temperature with 48 mW of 647.1 nm excitation.

Acknowledgment. We thank the National Science Foundation at Indiana University and The Ohio State University, the Engineering and Physical Sciences Research Council, and the University of London Intercollegiate Research Service for financial support. The Ohio Supercomputer Center is gratefully acknowledged for computational resources with which the DFT calculations were performed.

Supporting Information Available: Analysis of X-ray powder diffraction data (PDF). This material is available free of charge via the Internet at <http://pubs.acs.org>.

JA020248J

- (28) Becke, A. D. *Phys. Rev. A* **1988**, *38*, 3098–3100.
- (29) Becke, A. D. *J. Chem. Phys.* **1993**, *98*, 5648–5652.
- (30) Lee, C.; Yang, W.; Parr, R. G. *Phys. Rev. B* **1988**, *37*, 785–789.
- (31) Hehre, W. J.; Radom, L.; Schleyer, P. v. R.; Pople, J. A. *Ab initio Molecular Orbital Theory*; John Wiley & Sons: New York, 1986.
- (32) Andrae, D.; Hauessermann, U.; Dolg, M.; Stoll, H.; Preuss, H. *Theor. Chim. Acta* **1990**, *77*, 123–141.
- (33) Perdew, J. P.; Wang, Y. *Phys. Rev. B* **1992**, *45*, 13244.
- (34) Perdew, J. P.; Chevary, J. A.; Vosko, S. H.; Jackson, K. A.; Pederson, M. R.; Singh, D. J.; Fiolhais, C. *Phys. Rev. B* **1992**, *46*, 6671–6687.
- (35) van Lenthe, E.; Baerends, E. J.; Snijders, J. G. *J. Chem. Phys.* **1993**, *99*, 4597–4610.
- (36) van Lenthe, E.; Baerends, E. J.; Snijders, J. G. *J. Chem. Phys.* **1994**, *101*, 9783–9792.
- (37) van Lenthe, E.; Snijders, J. G.; Baerends, E. J. *J. Chem. Phys.* **1996**, *105*, 6505–6516.
- (38) van Lenthe, E.; van Leeuwen, R.; Baerends, E. J.; Snijders, J. G. *Int. J. Quantum Chem.* **1996**, *57*, 281–293.
- (39) van Lenthe, E.; Ehlers, A.; Baerends, E. J. *J. Chem. Phys.* **1999**, *110*, 8943–8953.
- (40) *GaussView 2.1*; Gaussian Inc.: Pittsburgh, PA, 1998.